Research in Astronomy and Astrophysics, 25:055022 (9pp), 2025 May

https://doi.org/10.1088/1674-4527/adcc7c
CSTR: 32081.14.RAA.adcc7c

The Photosphere Evolution, the Energy Sources, and the Early-time Excess of PTF11rka

Liu-Yi Wang (王浏毅)[1], Shan-Qin Wang (王善钦)[1], Tao Wang (王涛)[2], Deng-Wang Shi (石登旺)[3], Wen-Pei Gan (甘文沛)[4], and En-Wei Liang (梁恩维)[1]
[1] Guangxi Key Laboratory for Relativistic Astrophysics, School of Physical Science and Technology, Guangxi University, Nanning 530004, China; shanqinwang@gxu.edu.cn
[2] Department of Astronomy, Beijing Normal University, Beijing 100875, China
[3] Development and Reform Bureau of Sanjiang Dong Autonomous County, Liuzhou 545500, China
[4] Nanjing Hopes Technology Co., Ltd. Nanjing 210000, China
Received 2025 January 29; revised 2025 March 26; accepted 2025 March 31; published 2025 May 21

Abstract

In this paper, we determine the photosphere evolution of PTF11rka which is a type Ic supernova (SN) by fitting its spectral energy distributions at different epochs. We find that the photosphere of PTF11rka expanded at a constant velocity at early epochs, and the photosphere temperature increased slightly after reaching a minimum. These features are reminiscent of those of SN 2017dio. Based on the photosphere module that can describe the photosphere evolution of PTF11rka, we use the ^{56}Ni cascade decay model to fit its multiband light curves (LCs), finding that the model can well fit the photometric data. The derived ejecta mass and ^{56}Ni mass are respectively 8.76 $M_{\odot}$and 0.29−0.41 $M_{\odot}$; the derived peak luminosity and the rise time of the theoretical bolometric LC of PTF11rka are $\sim 8.24 \times 10^{42}$ erg s^{-1} and $\sim$ 35 days, respectively. Moreover, we find that the theoretical multiband LCs and the theoretical bolometric LC of PTF11rka do not show early-time excesses proposed in the literature. This indicates that additional energy sources (e.g., the interaction between the ejecta and the circumstellar material) suggested to be responsible for the early-time excess can be neglected.

Key words: (stars:) supernovae: general – (stars:) supernovae: individual (PTF11rka) – stars: evolution

1. Introduction

Core-collapse supernovae (CCSNe) originate from the explosions of massive stars with zero age main sequence (ZAMS) masses $\gtrsim 9\,M_{\odot}$ (Heger et al. 2003), leaving neutron stars (NSs) or black holes (BHs) at the center (Woosley et al. 2002). Thermonuclear SNe originate from the explosions of white dwarfs (WDs), leaving no compact remnant. Based on their features of peak spectra, SNe can be classified as types I (hydrogen-poor) and II (hydrogen-rich) (Minkowski 1941). Type I SNe are subdivided into type Ia which show strong silicon lines and weak helium lines in their spectra, type Ib which show strong helium lines in their spectra, and type Ic which show weak helium lines in their spectra (Filippenko 1997; Gal-Yam 2017). It is believed that the progenitors of type Ic SNe had lost their hydrogen envelopes and most of their helium envelopes before their explosions, while the progenitors of type Ib SNe retain a larger fraction of helium envelopes than those of SNe Ic. A fraction of type Ic SNe are broad-lined Ic SNe (SNe Ic-BL), some of which are associated with gamma-ray bursts (GRBs, Woosley & Bloom 2006; Hjorth & Bloom 2012; Cano et al. 2017).

According to their peak luminosities, SNe can be classified into normal-luminosity SNe, luminous SNe, and superluminous SNe (SLSNe; Gal-Yam 2012, 2019). The main energy source of normal-luminosity SNe is the ^{56}Ni cascade decay (Arnett 1982), while almost all luminous SNe and SLSNe might be mainly powered by the magnetar spinning-down (Kasen & Bildsten 2010; Woosley 2010; Inserra et al. 2013; Nicholl et al. 2013) or the interaction between the SN ejecta and the circumstellar material (CSM; Chevalier 1982; Chevalier & Fransson 1994; Chatzopoulos et al. 2012).

In the past years, some SNe Ib and Ic (e.g., SN 2017dio, Kuncarayakti et al. 2018; SN 2017ens, Chen et al. 2018; SN 2019ehk, Jacobson-Galán et al. 2020) showing evidence of early-time or late-time interaction between the SN ejecta and the CSM have been confirmed. PTF11rka is also a type Ic SN which is suggested to interact with CSM at early epochs (Pian et al. 2020, hereafter P20). PTF11rka was discovered by the Palomar Transient Factory (PTF; Law et al. 2009; Rau et al. 2009) on 2011 December 7 UT. The redshift (z) of PTF11rka is 0.0744 (P20). By adopting the assumption that the difference between bolometric magnitude and the $R_{\rm PTF}$ magnitude is a constant, P20 constructed the early-time bolometric light curve (LC). After fitting the bolometric LC of PTF11rka using the ^{56}Ni model, they found that the early bolometric luminosities are significantly higher than the theoretical bolometric LC produced by the ^{56}Ni model. They suggested that the early-time

excess of the bolometric LC of PTF11rka might be due to the early-time interaction between the SN ejecta and the CSM.

As pointed out by P20, however, the assumption P20 adopted to construct the bolometric LC might be unreliable. The SN temperature changes (usually decreases) during the early epochs, so the peaks of spectral energy distributions (SEDs) shift to red bands from blue bands, and the ratios between the flux in all bands and the total flux vary with time, i.e., the difference between magnitudes in all bands and the bolometric magnitudes varies with time. Hence, we also suggest that the assumption that $M_{\rm bol} - M_{R_{\rm PTF}}$ is constant in the early epochs might be unreliable, and that the bolometric luminosities of PTF11rka at early epochs might be overestimated.

We suggest that the energy sources and the physical properties of PTF11rka deserve further study. These are the aims of this paper. In Section 2, we determine the photosphere module of PTF11rka and derive the physical properties of PTF11rka by fitting the multiband LCs using the ^{56}Ni model. In Sections 3 and 4, we discuss our results and draw some conclusions.

2. Modeling the Multiband LCs of PTF11rka

2.1. The SEDs, the Temperature Evolution and the Radius Evolution of PTF11rka

Since only $R_{\rm PTF}$ photometry is available at early epochs, a bolometric LC cannot be synthesized directly. Therefore, we model the multiband LCs of PTF11rka. The method of fitting multiband LCs does not rely on pseudo-bolometric LCs constructed by using various assumptions (Nicholl et al. 2017), and can be used to fit the photometric data at the early epochs when only data in one band or two bands are available (see Nicholl et al. 2017 for the cases of type I SLSNe).

The fitting of multiband LCs needs reliable photosphere modules which present the evolution of the temperature and the radius of the photosphere of SNe and other optical transients. The photosphere module proposed by Nicholl et al. (2017) is widely used to fit the multiband model LCs of SLSNe and tidal disruption events. This photosphere module assumes that both the photospheric velocity at the early epochs and the temperature at the late epochs are constant (Nicholl et al. 2017).

However, Wang et al. (2023) found that the photospheric velocity of SN 2018gk at the early epochs can be divided into two episodes having different values. Besides, the temperature of some SNe at the late epochs increased (linearly) (see, e.g., Figure 4 of Prentice et al. 2019, Figure 3 of Pandey et al. 2021, and Figure 1 of Shi et al. 2024). To obtain the photosphere module which can describe the photosphere evolution of PTF11rka, we fit the SEDs at the epochs having data in at least three bands with time intervals within 0.1 days using the ultraviolet (UV)-absorbed blackbody model (Nicholl et al. 2017; Prajs et al. 2017)

$$F_\nu = \begin{cases} \dfrac{\lambda}{\lambda_{\rm CF}} \dfrac{2\pi h\nu^3}{c^2} (e^{\frac{h\nu}{k_{\rm b}T_{\rm ph}}} - 1)^{-1} \dfrac{R_{\rm ph}^2}{D_L^2}, & \lambda \leqslant \lambda_{\rm CF} \\ \dfrac{2\pi h\nu^3}{c^2} (e^{\frac{h\nu}{k_{\rm b}T_{\rm ph}}} - 1)^{-1} \dfrac{R_{\rm ph}^2}{D_L^2}, & \lambda > \lambda_{\rm CF} \end{cases}, \quad (1)$$

where $\lambda_{\rm CF} = 3000$ Å is the cutoff wavelength, and $D_{\rm L}$ is the luminosity distance of the SN. We remove the data at two epochs (MJD 55958.30 and 56085.26−56085.30) since the three bands are in $R_{\rm PTF}$, r, and i, which cannot be used to constrain the short wavelength regime of the blackbody model curve. The UV-absorbed blackbody fits for the SEDs at 25 epochs are shown in Figure A1.

The curves which describe the evolution of the temperature and the radius of the photosphere of PTF11rka are displayed in Figure 1. We find that a constant velocity of $\sim 0.82 \times 10^9$ cm s^{-1} best describes the photosphere radius at the early epochs (see the red dashed line in the top-left panel of Figure 1). However, the temperature evolution of PTF11rka cannot be described by Nicholl et al. (2017)'s photosphere module which assumes a temperature floor, since it increases after reaching its minimum. This means that it is necessary to modify the photosphere module. Therefore, we assume that the temperature evolution can be described by a linear function and find the slope of ~ 7.87 K day^{-1} (see the red dashed line in the top-right panel of Figure 1) can best describe the evolution of the photosphere temperature. These features are similar to those of SN 2012au (Pandey et al. 2021) and SN 2017dio (Shi et al. 2024).

Therefore, we adopt the photosphere module proposed by Shi et al. (2024) to describe the photosphere temperature of PTF11rka

$$T_{\rm ph}(t) = \begin{cases} \left(\dfrac{L_{\rm SN}(t)}{4\pi\sigma v_{\rm ph}^2 t^2}\right)^{\frac{1}{4}}, & t \leqslant t_b \\ \alpha_{\rm pb}(t - t_b) + T_b, & t > t_b \end{cases}, \quad (2)$$

where $L_{\rm SN}(t)$ is the bolometric luminosity of the SN, σ is the Stefan-Boltzmann constant, $v_{\rm ph}$ is the early-time photospheric velocity, $\alpha_{\rm pb}$ is the slope after reaching the lowest temperature, t_b is the moment when reaching the lowest temperature, and T_b is the lowest photosphere temperature. The radius evolution function can be described by the equation

$$R_{\rm ph}(t) = \begin{cases} v_{\rm ph} t, & t \leqslant t_b \\ \left(\dfrac{L_{\rm SN}(t)}{4\pi\sigma[\alpha_{\rm pb}(t - t_b) + T_b]^4}\right)^{\frac{1}{2}}, & t > t_b \end{cases}. \quad (3)$$

2.2. Fitting the Multiband LCs of PTF11rka Using the ^{56}Ni Model

The explosions of CCSNe synthesize a large amount of ^{56}Ni which can decay to ^{56}Co and then ^{56}Fe. It is widely believed

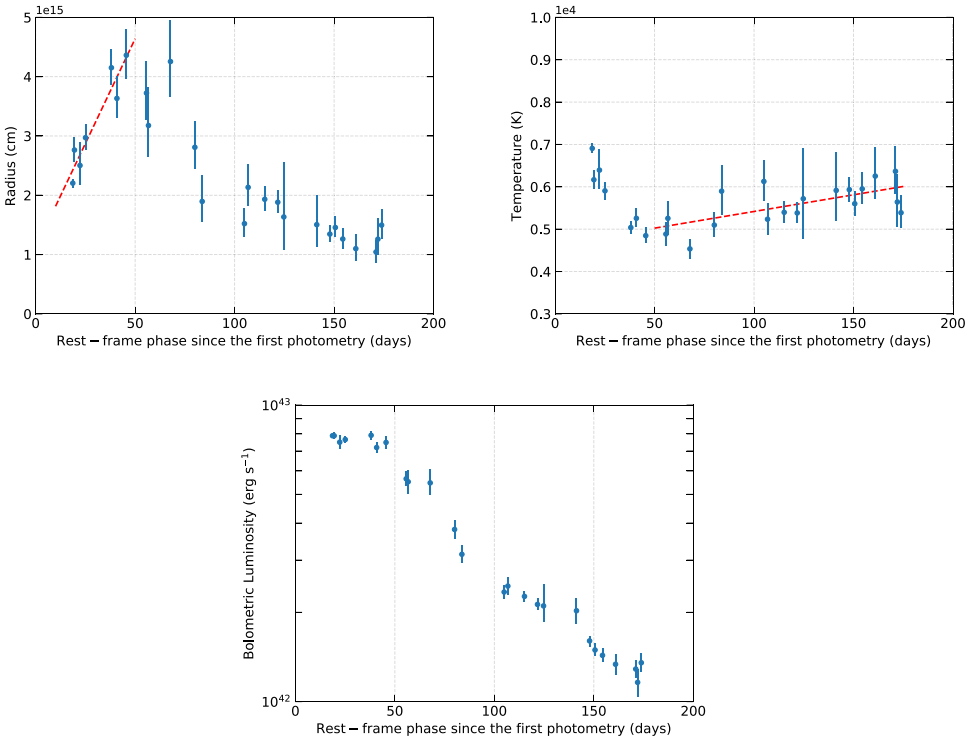

Figure 1. The radius evolution (top left), the temperature evolution (top right), and the bolometric luminosity (bottom).

that the cascade decay of ^{56}Ni can power the bolometric LCs ($L_{\rm SN}(t)$) of normal SNe I (including Ia, Ib, and Ic). In this scenario, the LCs of SNe are powered by the energy deposition of gamma-rays from the ^{56}Ni cascade decay (^{56}Ni→^{56}Co→^{56}Fe) and the electron-positron annihilation and the kinetic energy of the positrons (Sutherland & Wheeler 1984; Cappellaro et al. 1997; Valenti et al. 2008). Therefore, we use the ^{56}Ni model (Arnett 1982; Valenti et al. 2008) to fit the LCs of PTF11rka.[5] The details of the ^{56}Ni model can be found in Wang et al. (2023) and references therein.[6] The definitions, units, and priors of the parameters of the ^{56}Ni model are listed in Table 1. The Markov Chain Monte Carlo (MCMC) as implemented by the `emcee` Python package (Foreman-Mackey et al. 2013) is used to derive the medians, the 1σ bounds, and the best-fitting values of all parameters.

The fit of the ^{56}Ni model is depicted in Figure 2 which affirms that the multiband LCs of PTF11rka can be well fitted by the model. The corresponding corner plot is presented in Figure A2 in the Appendix. The medians, 1σ bounds, and best-fitting values of all parameters are listed in Table 1. The best-fitting parameters of the ^{56}Ni model are

$M_{\rm ej} = 8.76\ M_\odot$, $v_{\rm ph} = 0.86 \times 10^9\ {\rm cm\ s^{-1}}$, $M_{\rm Ni} = 0.70\ M_\odot$, $\log \kappa_{\gamma,{\rm Ni}} = -1.39\ {\rm cm^2\ g^{-1}}$, $\kappa_{\rm e}^{+} = 8.99\ {\rm cm^2\ g^{-1}}$, $t_{\rm b} = 58.75$ days, $\alpha_{\rm pb} = 6.75\ {\rm K\ day^{-1}}$,[7] $t_{\rm shift} = -9.96$ days.

3. Discussion

3.1. The Bolometric LC and the Physical Properties of PTF11rka

To obtain the theoretical bolometric LC of PTF11rka, we integrate the SEDs ($L_{\rm ph} = \int_0^\infty F_\nu d\nu$) at all epochs constructed from the theoretical multiband LCs produced by the best-fitting parameters (see Figure 3). The peak luminosity ($L_{\rm p}$) and the rise time ($t_{\rm p}$) of the theoretical bolometric LC are $\sim$8.24 $\times$ 10^{42} erg s^{-1} and $\sim$35 days respectively. The former is lower than the value derived by P20 ($\sim 10^{43}$ erg s^{-1}), while the latter is larger than the value given by P20 ($\sim$30 days).

[5] This model assumed that the ^{56}Ni distribution peaked toward the center of the ejecta and it neglected the effect of the spatial distribution of ^{56}Ni that could change the LC of SNe.

[6] There is a typo in Section 2.1 of Wang et al. (2023), i.e., $\mathcal{E}_{\rm Co} = \epsilon_{\rm Co} M_{\rm Ni} e^{-t/\tau_{\rm Co}} - e^{-t/\tau_{\rm Ni}}$ should be replaced by $\mathcal{E}_{\rm Co} = \epsilon_{\rm Co} M_{\rm Ni} (e^{-t/\tau_{\rm Co}} - e^{-t/\tau_{\rm Ni}})$.

[7] This value is slightly different from that ($\sim$7.87 K day^{-1}) derived in Section 2.1. This is because the value of 7.87 was derived based on the fitting for the SEDs at epochs having photometry in at least three bands, while the value of 6.75 K day^{-1} was derived based on the multiband fits for all data which not only included the three- or four-band SEDs, but also the epochs having photometry in only one or two band(s) (e.g., the data at about 100 days and the last two epochs).

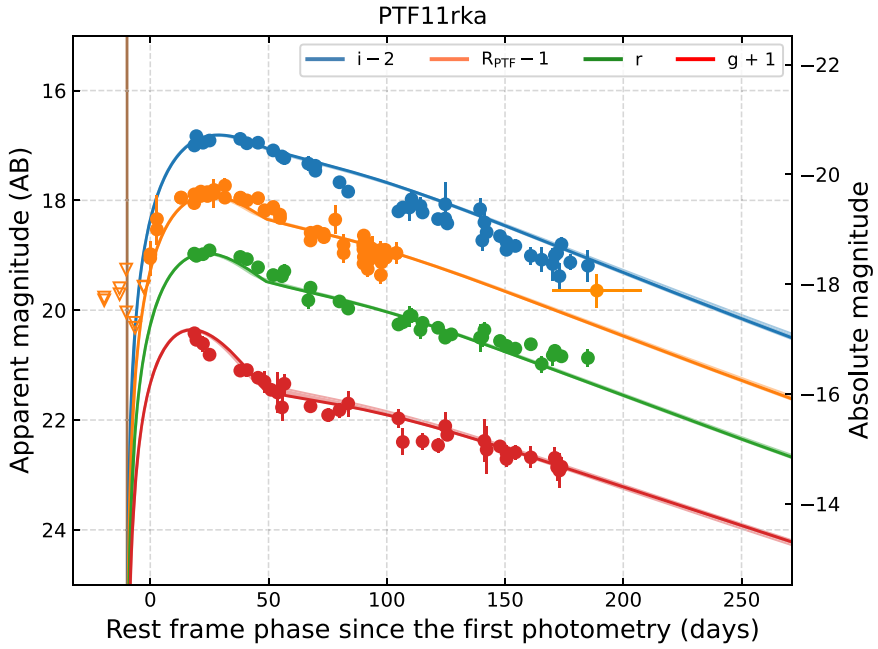

Figure 2. The best fits of the multiband LCs of PTF11rka using the ^{56}Ni model. The data are from Table 1 of P20, where triangles represent upper limits. The $R_{\rm PTF}$ data between days 170 and 200 have been averaged (P20).

Table 1
Definitions, Units, Priors, Medians, 1σ Bounds, and Best-fitting Values for the Parameters of the ^{56}Ni model

Parameter	Definition	Unit	Prior	Best Fit	Median
$M_{\rm ej}$	The ejecta mass	$M_\odot$	[0.1, 50]	8.76	$8.56^{+0.34}_{-0.33}$
$v_{\rm ph}$	The early-time photospheric velocity	10^9 cm s^{-1}	[0.6, 1.2]	0.86	$0.87^{+0.03}_{-0.02}$
$M_{\rm Ni}$	The ^{56}Ni mass	$M_\odot$	[0, 1.0]	0.70	$0.69^{+0.01}_{-0.01}$
$\log \kappa_{\gamma,{\rm Ni}}$	The γ-ray opacity	cm^2 g^{-1}	[−1.57, 4]	−1.39	$-1.36^{+0.05}_{-0.03}$
κ_{e^+}	The positron opacity	cm^2 g^{-1}	[4, 14]	8.99	$8.94^{+3.43}_{-3.37}$
$t_{\rm b}$	The temperature break time	day	[45, 60]	58.75	$57.04^{+1.85}_{-4.20}$
$\alpha_{\rm pb}$	The slope after the temperature break	K day^{-1}	[0, 15]	6.75	$5.91^{+1.25}_{-1.53}$
$t_{\rm shift}$	The explosion time relative to the first data	day	[−10, 0]	−9.96	$-9.86^{+0.21}_{-0.10}$

Our derived ejecta mass is 8.76 $M_\odot$, which is comparable to the value of P20 (∼8 $M_\odot$). The value of $v_{\rm ph}$ is 8600 km s^{-1}, which is lower than the best-fitting value (12,500 km s^{-1}) of the photospheric velocity derived from the spectra at +20 days (P20). For most SNe, the early-time photospheric velocities derived by the blackbody model are lower than those derived by the early-time spectra. At the late epochs, the photospheric velocities derived by the blackbody model are negative since the photospheres recede, while the photospheric velocities derived by the spectra are positive. Therefore, the discrepancy between the two values is reasonable.

The best-fitting value of $M_{\rm Ni}$ is 0.70 $M_\odot$. As pointed out by Khatami & Kasen (2019), however, Arnett's model may overestimate the ^{56}Ni masses of stripped envelope SNe, and more reasonable ^{56}Ni masses can be derived using the equation (Khatami & Kasen 2019)

$$M_{\rm Ni} = \frac{L_{\rm p}\beta^2 t_{\rm p}^2}{2\epsilon_{\rm Ni}\tau_{\rm Ni}^2}\left(\left(1-\frac{\epsilon_{\rm Co}}{\epsilon_{\rm Ni}}\right)(1-(1+\beta t_{\rm p}/\tau_{\rm Ni})e^{-\beta t_{\rm p}/\tau_{\rm Ni}}) + \frac{\epsilon_{\rm Co}\tau_{\rm Co}^2}{\epsilon_{\rm Ni}\tau_{\rm Ni}^2}(1-(1+\beta t_{\rm p}/\tau_{\rm Co})e^{-\beta t_{\rm p}/\tau_{\rm Co}})\right)^{-1}, \quad (4)$$

where $\epsilon_{\rm Ni} = 3.9\times10^{10}$ erg s^{-1} g^{-1} is the energy generation rate of ^{56}Ni; $\epsilon_{\rm Co} = 6.78\times10^{9}$ erg s^{-1} g^{-1} is the energy generation rate of ^{56}Co; $\tau_{\rm Ni} = 8.8$ days is the lifetime of the ^{56}Ni; $\tau_{\rm Co} = 111.3$ days is the lifetime of the ^{56}Co (Sutherland

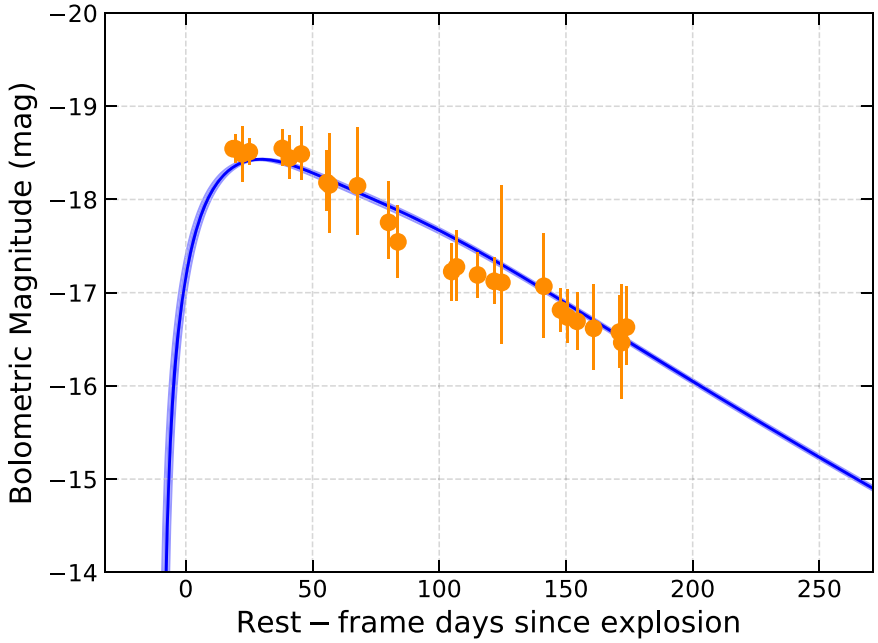

Figure 3. The bolometric LC of PTF11rka derived by the best-fitting parameters of the ^{56}Ni model. The shaded region indicates 1σ errors of the parameters. Also plotted is the bolometric LC derived by SED fits.

& Wheeler 1984; Cappellaro et al. 1997); the values of β are 0.88 and 0.56 for normal Ic and Ic-BL SNe, respectively (Afsariardchi et al. 2021). The ^{56}Ni mass obtained using Equation (4) is 0.41 $M_{\odot}$ or 0.29 $M_{\odot}$ for normal Ic or Ic-BL SNe, respectively. We suggest that the ^{56}Ni mass of PTF11rka is between 0.29 $M_{\odot}$ and 0.41 $M_{\odot}$, since the properties of PTF11rka lie between those of normal and Ic-BL SNe (P20). The ^{56}Ni mass derived here (0.29−0.41 $M_{\odot}$) is lower than the value derived by P20 (∼0.5 $M_{\odot}$).

3.2. The Early-time Excess of the Bolometric LC

The bolometric LC of PTF11rka constructed by P20 shows an early-time excess which cannot be explained by the ^{56}Ni model. P20 attributed it to the early-time interaction between the SN ejecta and the CSM (CSI). Some SNe (e.g., SN 2019ehk, Jacobson-Galán et al. 2020) had been confirmed to experience CSI at early epochs, since their early-time LCs exhibit bumps and their early spectra display strong emission lines indicative of CSI. However, the multiband LCs of PTF11rka do not show bumps throughout its evolution. Additionally, the method of constructing the early bolometric LC adopted by P20 is based on the assumption that the difference between the bolometric magnitudes ($M_{\rm bol}$) and the $R_{\rm PTF}$ magnitudes ($M_{R_{\rm PTF}}$) is constant throughout the early epochs.

As pointed out by P20, however, this assumption might be unreliable. Moreover, our SED fits show that the temperature decreased during the early epochs (see Figure 1), so the SED peaks shifted to redder bands as the SN evolved, and the ratio between $R_{\rm PTF}$ flux and the bolometric flux (the difference between magnitudes in each band and the bolometric magnitudes) varied. Hence, the assumption that $M_{\rm bol} - M_{R_{\rm PTF}}$ is constant in the early epochs is unreliable for PTF11rka.

The multiband LC fits do not require constructed bolometric LCs, and therefore do not rely on the assumptions (e.g., the assumption mentioned above) used to construct them. Furthermore, the multiband LC fits can utilize the early-time photometric data at one band, which not only play a key role for determining the explosion date of an SN, but also constrain the early-time LC evolution of the SN.

Our fit shows that the ^{56}Ni model can match the multiband LCs of PTF11rka without introducing early-time CSI, suggesting that PTF11rka is an SN that is not interacting with CSM, or the interaction between ejecta and the CSM can be neglected.

3.3. The Late-time Temperature Rise of PTF11rka

Besides PTF11rka, some stripped envelope SNe (Ib, Ic, and IIb) also show temperature rise (Ergon et al. 2014; Prentice et al. 2019; Pandey et al. 2021; Shi et al. 2024). Prentice et al. (2019) suggested that the apparent rise in temperature of stripped envelope SNe in their sample is unlikely to be real, as the SEDs deviated from thermal ones and the photosphere had disappeared.

However, some SNe Ic and Ib show temperature rise at rather early epochs (as early as 20 days after the explosion for

SN 2017dio, see Figure 1 of Shi et al. 2024) when the SN photospheres might still exist, and the SEDs at these epochs can be fitted by the blackbody (thermal) model. Therefore, the possibility of that non-zero temperature slope for some SNe Ib and Ic (including PTF11rka) cannot be excluded.

For most SNe Ibc, the photospheres of SNe cool to constant temperatures (Nicholl et al. 2017) when the bolometric LCs decline and the photosphere recedes into the ejecta (due to recombination or other processes). The typical temperature of ∼6000 K could correspond to the fact that the recombination temperature of O II is ∼6000 K (Nicholl et al. 2017). Assuming that the late-time temperature rise of PTF11rka is real and was due to the recombination of some element (e. g., O I or O II), it indicates that the recombination that resulted in the photosphere recession was quicker than those of the SNe that show constant temperatures at the late epochs.

It should be noted that the slope of the late-time temperature curve of PTF11rka (∼6.75 K day^{-1}) is significantly smaller than those of SN 2011dh (∼12 K day^{-1}, estimated from Figure 5 of Ergon et al. 2014), SN 2012au (∼16 K day^{-1}, estimated from Figure 3 of Pandey et al. 2021), and SN 2017dio (∼40 K day^{-1}, Shi et al. 2024). Moreover, the SEDs of PTF11rka at the epochs 150 days after the explosion show excesses at the r band, indicating that the SED fits at these epochs might be unreliable. In addition, the uncertainties of the derived temperature at the epochs before 150 days can influence the derived slope.

These facts suggest that the temperature rise of PTF11rka might be negligible. We use the model assuming that the slope of the temperature curve is 0 to fit the multiband LCs of PTF11rka, finding that the fitting works as well as the non-zero slope. The value of χ^2/dof (3.86) is slightly larger than that (3.84) of the temperature rise model.

4. Conclusions

In this paper, we study the energy sources and physical properties of PTF11rka which is a type Ic SN. P20 suggested that it might interact with the CSM at the early epochs.

We fit the SEDs of PTF11rka, finding that the early-time velocity of its photosphere ($v_{\rm ph}$) is constant, while the late-time temperature increased linearly. These features are reminiscent of those of SN 2017dio. Therefore, we adopt the photosphere module proposed by Shi et al. (2024) which assumed that the temperature evolution can be described by a linear function.

Based on the modified photosphere module, we fit the multiband LCs of PTF11rka using the ^{56}Ni model. We find that the early-time LCs can be well fitted by this model. The value of $v_{\rm ph}$ is 0.86 × 10^9 cm s^{-1}, the slope of the linear function describing the late-time temperature evolution is 6.75 K day^{-1}, $M_{\rm ej}$ = 8.76 $M_\odot$, $M_{\rm Ni}$ = 0.70 $M_\odot$.

The derived slope of the temperature rise is significantly lower than those of the SNe which also show temperature rise. The fitting adopting a constant late-time temperature can obtain a result which is as good as the temperature rise model. This suggests that, while the temperature rise might be real, its effect on fitting the multiband LCs can be neglected.

We construct the theoretical bolometric LC using the best-fitting parameters, and find that its peak luminosity and rise time are ∼8.24 × 10^{42} erg s^{-1} and ∼35 days, respectively. Adopting the equation in Khatami & Kasen (2019) and the derived bolometric properties, the value of $M_{\rm Ni}$ is lowered to be 0.29–0.41$M_\odot$, which is lower than the value derived by P20.

Our derived bolometric LC also shows no early-time excess. This can be expected, since the multiband LCs do not show early-time excesses. This, together with the fact that the multiband LCs of PTF11rka can be explained by the ^{56}Ni model, suggests that, while there might be an interaction between the SN ejecta and the CSM at early epochs, its contribution to the multiband LCs (and therefore bolometric LC) can be neglected.

The early-time observations of most SNe are in one or two bands. It is difficult to construct precise early-time bolometric LCs for them. The assumption that the ratio of bolometric flux to some band is constant at the early epochs might be unreliable; this assumption might result in early-time bolometric LCs which deviated from the real ones, and might require additional energy sources to account for the deviations (for the cases showing excesses). Our result derived by the multiband fitting does not introduce the deviations, demonstrating the advantage of the multiband models which can play an important role in deriving the physical properties of optical transients (including SNe) and revealing their energy sources.

Acknowledgments

This work is supported by the National Natural Science Foundation of China (NSFC, grant Nos. 12494571, 11963001 and 12133003). This work is supported by the Program of Bagui Scholars (LHJ).

Appendix

Figures A1 and A2 present the UV-absorbed blackbody model for SEDs and the corner plot of the ^{56}Ni model for the multiband LCs of PTF11rka, respectively.

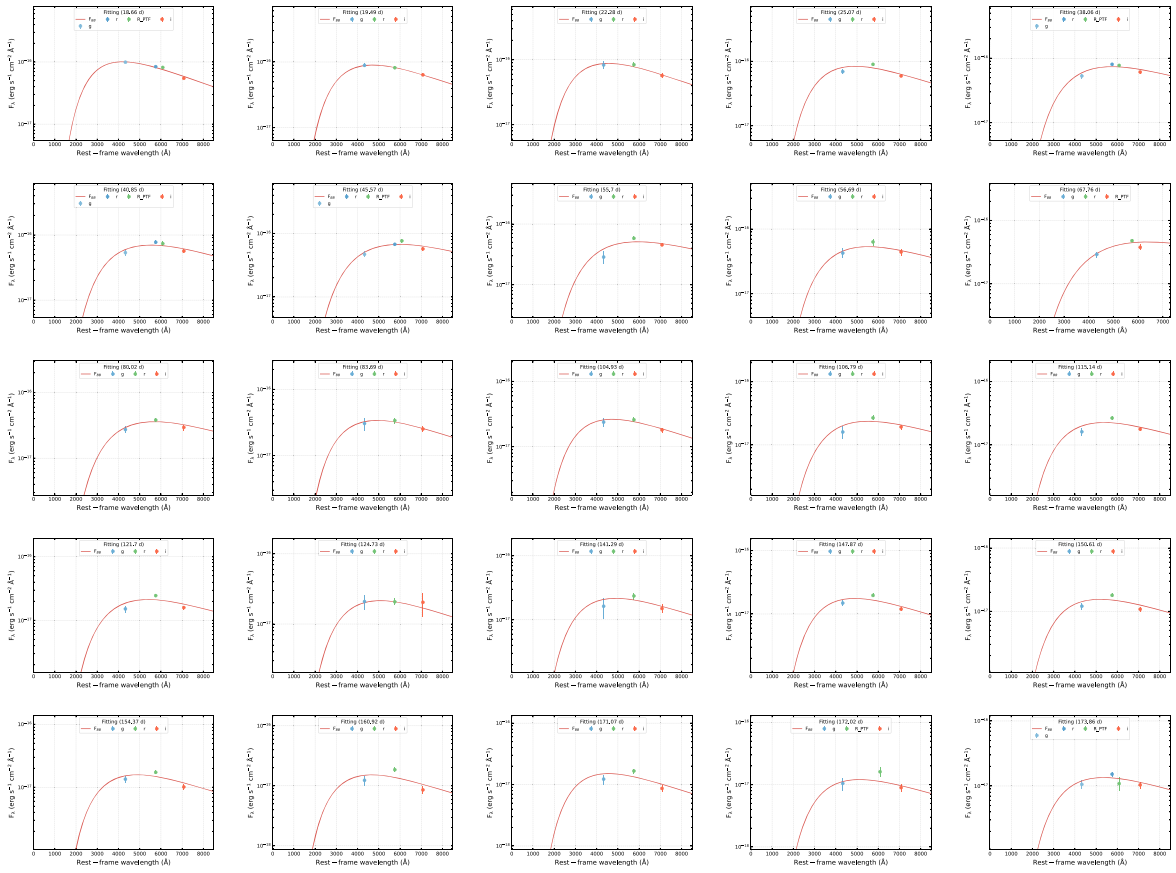

Figure A1. Fits of the UV-absorbed blackbody model for SEDs of PTF11rka. The data are from Table 1 of P20.

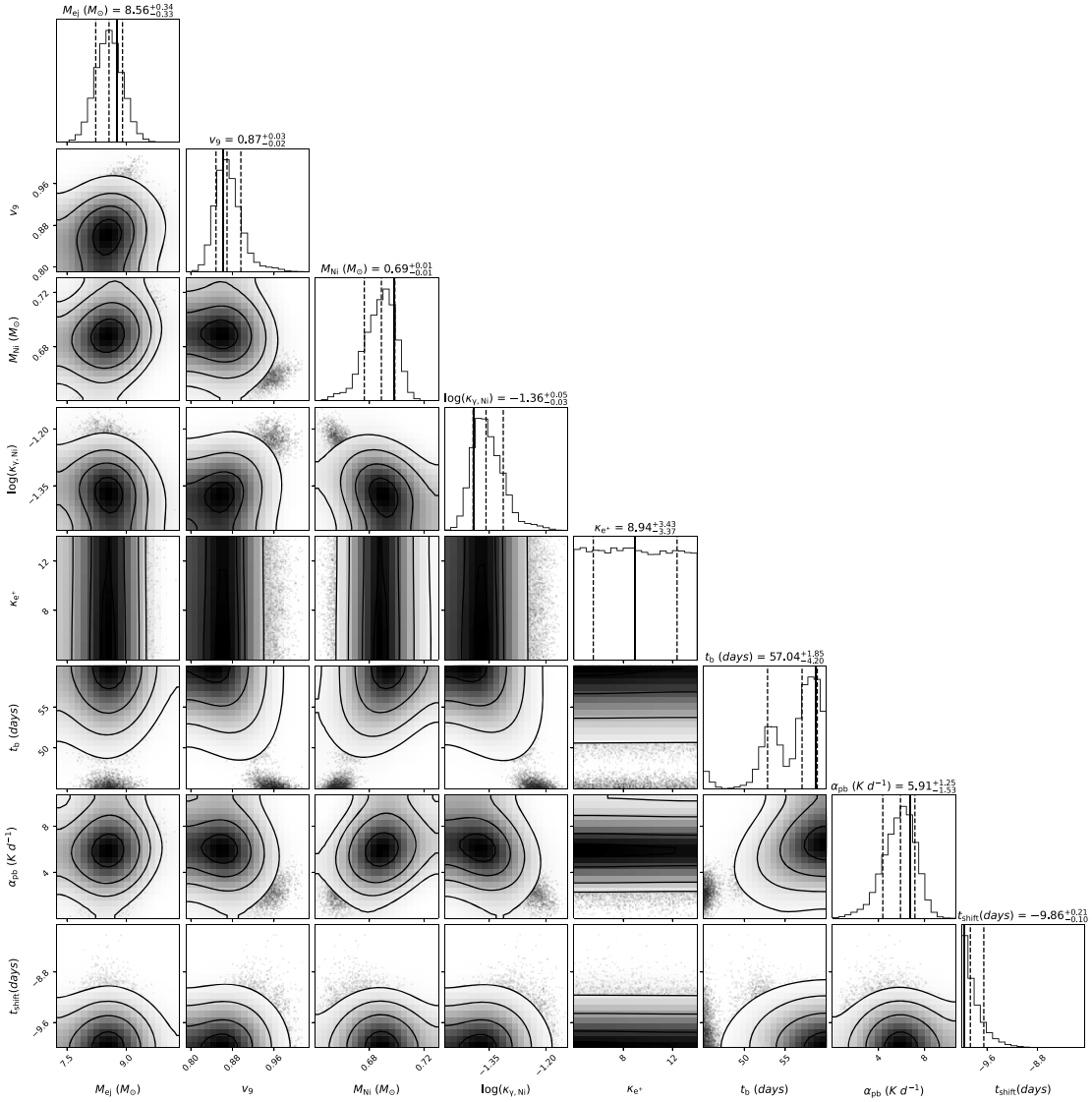

Figure A2. Corner plot of the ^{56}Ni model for the multiband LCs of PTF11rka. The solid vertical lines represent the best-fitting parameters, while the dashed vertical lines represent the medians and the 1σ bounds of the parameters.

References

Afsariardchi, N., Drout, M. R., Khatami, D. K., et al. 2021, ApJ, 918, 89
Arnett, W. D. 1982, ApJ, 253, 785
Cano, Z., Wang, S.-Q., Dai, Z.-G., et al. 2017, AdAst, 2017, 8929054
Cappellaro, E., Mazzali, P. A., Benetti, S., et al. 1997, A&A, 328, 203
Chatzopoulos, E., Wheeler, J. C., & Vinko, J. 2012, ApJ, 746, 121
Chevalier, R. A. 1982, ApJ, 258, 790
Chevalier, R. A., & Fransson, C. 1994, ApJ, 420, 268
Chen, T. W., Inserra, C., Fraser, M., et al. 2018, ApJL, 867, L31
Ergon, M., Sollerman, J., Fraser, M., et al. 2014, A&A, 562, A17
Filippenko, A. V. 1997, ARA&A, 35, 309
Foreman-Mackey, D., Hogg, D. W., Lang, D., et al. 2013, PASP, 125, 306
Gal-Yam, A. 2012, Sci, 337, 927
Gal-Yam, A. 2017, Handbook of Supernovae (Berlin: Springer), 195
Gal-Yam, A. 2019, ARA&A, 57, 305
Heger, A., Fryer, C. L., Woosley, S. E., Langer, N., & Hartmann, D. H. 2003, ApJ, 591, 288
Hjorth, J., & Bloom, J. S. 2012, in Gamma-Ray Bursts, ed. C. Kouveliotou, R. A. M. J. Wijers, & S. Woosley (Cambridge: Cambridge Univ. Press), 169
Inserra, C., Smartt, S. J., Jerkstrand, A., et al. 2013, ApJ, 770, 128
Jacobson-Galán, W. V., Margutti, R., Kilpatrick, C. D., et al. 2020, ApJ, 898, 166
Kasen, D., & Bildsten, L. 2010, ApJ, 717, 245
Kuncarayakti, H., Maeda, K., Ashall, C. J., et al. 2018, ApJL, 854, L14
Khatami, D. K., & Kasen, D. N. 2019, ApJ, 878, 56
Law, N. M., Kulkarni, S. R., Dekany, R. G., et al. 2009, PASP, 121, 1395
Minkowski, R. 1941, PASP, 53, 224
Nicholl, M., Guillochon, J., & Berger, E. 2017, ApJ, 850, 55
Nicholl, M., Smartt, S. J., Jerkstrand, A., et al. 2013, Natur, 502 346
Pandey, S. B., Kumar, A., Kumar, B., et al. 2021, MNRAS, 507, 1229
Pian, E., Mazzali, P. A., Moriya, T. J., et al. 2020, MNRAS, 497, 3542
Prajs, S., Sullivan, M., Smith, M., et al. 2017, MNRAS, 464, 3568
Prentice, S. J., Ashall, C., James, P. A., et al. 2019, MNRAS, 485, 1559
Rau, A., Kulkarni, S. R., Law, N. M., et al. 2009, PASP, 121, 1334
Shi, D. W., Wang, S. Q., Gan, W. P., et al. 2024, ApJ, 969, 32
Sutherland, P. G., & Wheeler, J. C. 1984, ApJ, 280, 282
Valenti, S., Benetti, S., Cappellaro, E., et al. 2008, MNRAS, 383, 1485
Wang, T., Wang, S. Q., Gan, W. P., & Li, L. 2023, ApJ, 948, 138
Woosley, S. E. 2010, ApJL, 719, L204
Woosley, S. E., & Bloom, J. S. 2006, ARA&A, 44, 507
Woosley, S. E., Heger, A., & Weaver, T. A. 2002, RvMP, 74, 1015